

and transport of water within Nafion has been extensively studied. A survey of this literature demonstrates that water transport in Nafion can be affected by membrane thickness,^{20,21,23} annealing conditions,^{18,19,29} processing methodologies,^{30–32} and water vapor concentration.^{15,33} However, the aforementioned body of work has largely focused on bulk membranes, and there is a general lack of knowledge on the response of Nafion at interfaces and confined to very thin films or layers. While bulk Nafion transport properties are relevant for the active membrane layer within the membrane electrode assembly (MEA) in a fuel cell, this complex polyelectrolyte is also used as an ionically conductive binder in the electrode and catalyst layer. It has been shown that in these composite electrodes Nafion is heterogeneously dispersed and often confined to films that are on the order of 2–10 nm thick.^{34,35} It is known that polymer confinement can affect both morphology³⁶ and chain dynamics³⁷ and, therefore, material properties such as the glass transition,³⁸ solute sorption,^{19,39,40} and mechanical properties.^{37,41–46} The structure, transport, and performance properties of Nafion confined near an interface—as it exists at within the catalyst layer of the MEA—have received little attention. This interfacial boundary region of the fuel cell is critical to the performance of the entire fuel cell as it mediates the transport of reactant gases, ions, electrons, and water. Simulations of water, proton, and reactant gas diffusion within a catalyst layer are powerful tools to predict and optimize fuel cell performance; however, all of these simulations are based on bulk membrane properties.^{34,47,48} A limited number of studies have demonstrated deviations in either the morphology,^{49–53} water (or solute) sorption,^{19,54–57} or proton conductivity^{58,59} from their bulk values in Nafion thin films. This raises the issue of whether it is appropriate to use the bulk properties of Nafion when modeling its behavior within the catalyst layer. However, these studies lack a systematic and comprehensive investigation of these properties to establish broad, fundamental insight into the structure–property relationships in these polyelectrolyte thin films. There exists a need to characterize the interdependence of the morphology, proton conductivity, mechanical properties, swellability, and water transport of Nafion under confinement near an interface in order to more accurately model the performance of the MEA in a working fuel cell.

This work focuses on the water absorption and transport in Nafion thin films (20–222 nm) cast onto silicon substrates. While these properties have been studied in detail for bulk membranes, very little is known about their behavior in thin films or at interfaces. These planar films serve as a model system for the confined thin films of Nafion on the catalyst particles and carbon supports in the electrode layer of a MEA. Utilizing specular X-ray reflectivity (SXR), neutron reflectivity (NR), grazing-incidence small-angle X-ray scattering (GISAXS), polarization-modulation infrared reflection–absorption spectroscopy (PM-IRRAS), and quartz-crystal microbalance (QCM) measurements, we have measured the structure, water content, extent of swelling, and effective diffusion coefficients of water in Nafion thin films exposed to water vapor. These studies are a step toward a comprehensive understanding of how the material properties of Nafion, germane to fuel cell performance, behave under confinement. This insight has the potential to provide a deeper understanding into the origins of fuel cell performance loss due to mass transport limitations within the catalyst layer.

■ EXPERIMENTAL METHODS

Film Preparation for Specular X-ray Reflectometry (SXR). A series of Nafion dispersions were prepared for spin-coating films onto silicon wafers. Nafion stock solution (20% by mass in water, alcohol, and ether mixture purchased from Aldrich) was diluted to varied extents with anhydrous ethanol (1:20 to 1:4 by volume) to obtain concentrations appropriate for film thicknesses in the range of approximately 20–222 nm. The solutions were mixed thoroughly before spin-coating. Silicon wafers were washed with toluene and acetone and then dried with a dry nitrogen jet. Wafers were then placed in an Anatech SP100-QTZ plasma etcher for 5 min at ~60 W. The Nafion solutions were immediately cast onto the cleaned silicon wafers at a spinning rate of 2000–3500 rpm to obtain films of the desired thickness. Films were then stored under ambient conditions until needed, but for no more than 48 h.

Film Preparation for Polarization-Modulation Infrared Reflection–Absorption Spectroscopy (PM-IRRAS). Phosphorus-doped, double-side-polished, silicon wafers, reported by the vendor to have a thickness of $500 \pm 25 \mu\text{m}$ and resistivity of $15 \pm 5 \text{ ohm}\cdot\text{cm}$ (for high infrared transparency), were purchased from Silicon Quest International and used for the supporting substrates in the PM-IRRAS diffusion studies. One side of the polished silicon wafer was coated with a $5 \pm 0.5 \text{ nm}$ chromium adhesion layer and a $100 \pm 2 \text{ nm}$ gold layer as an infrared reflective mirror. Each metal layer was deposited via metal evaporation under reduced pressure, and the thickness was measured using a quartz crystal microbalance. Nafion films were cast on the opposite side of the silicon wafer, i.e., the native oxide, per the procedures in the SXR film preparation.

SXR Sample Analysis. A Philips X'pert X-ray diffractometer was used to characterize the equilibrium film thickness and water content of Nafion thin films exposed to a series of water vapor concentrations. Reflectivity data were collected in the specular condition with the grazing incident angle equal to the detector angle. Data were collected over a specular angle range of 0.1° – 1.0° with a step size of 0.0003° . The tension and current of the X-ray source were set to 45 kV and 40 mA, respectively. The instrument was equipped with a temperature-controlled environmental chamber fitted with beryllium windows, a humidified air inlet, and an exhaust port with a humidity sensor. The vapor pressure of water within the sample chamber was controlled via an external mass flow device. Two mass flow controllers were connected in parallel and programmed to deliver a total flow rate of $500 \pm 5 \text{ mL/min}$. Controller A controlled the flow rate of dry air (0% RH) while controller B controlled the flow rate of humidified air. The air from controller B was humidified by bubbling dry air through deionized water. The vapor pressure of water within the X-ray sample chamber was adjusted by tuning the flow ratio of each controller, keeping the total flow rate at $500 \pm 5 \text{ mL/min}$. The humidity in the chamber was monitored using an in-situ temperature/humidity sensor with a precision of $\pm 2\%$ RH and $\pm 0.5^\circ\text{C}$, and it took approximately 20–30 min for the system to equilibrate after a change in the humidity set point. All measurements were done at ambient temperature ($27 \pm 0.5^\circ\text{C}$).

The samples were mounted onto the stage and enclosed with the X-ray transparent encasement. After mounting each sample, the Nafion films were dried under a continuous flow (500 mL/min) of dry air overnight at room temperature. The thickness, scattering length density, and surface roughness were determined by modeling based on the Parratt formalism⁶⁰ and the “reflpak” software was used to fit the data.^{61,62} Reflectivity data acquired immediately after drying were used to determine the initial, dry film thickness for each film. Films were then subjected to a series of humidified environments of increasing relative humidity ranging from 0% RH to 75% RH at $27 \pm 0.5^\circ\text{C}$. Samples were allowed to equilibrate for 1 h at each RH before collecting the SXR data. The sample equilibration time was determined from monitoring the critical edge and the first two interference fringes in the reflectivity data. After 1 h, no appreciable change in either the critical angle or the first two fringes was observed, implying that the samples had equilibrated with respect to absorbed

water and film swelling. Note that the sample equilibrated slower than the time for the humidity in the chamber to change.

Neutron Reflectivity. Neutron reflectivity (NR) was performed on the Advanced Neutron Diffractometer/Reflectometer (AND/R) at the National Institute of Standards and Technology (NIST) Center for Neutron Research.⁶³ The specularly reflected intensity was measured as a function of incident angle and then reduced through proper background subtraction. The resulting intensity was normalized by a slit scan to yield the reflectivity as a function of the scattering vector, Q . Modeling was carried out employing the Parratt formalism,⁶⁰ and the “reflpak” software was used to fit the data.⁶² During data collection, the sample temperature was kept constant to within ± 0.2 °C, and the dew point was controlled by a humidity generator with argon as a carrier gas. The temperature of the pathway where the gas mixture was delivered to the sample chamber was maintained above the dew point to avoid condensation. The relative humidity was recorded during data acquisition, but reported RHs were determined from the sample temperature and dew point.

Grazing Incidence Small-Angle X-ray Scattering. GISAXS experiments were performed at the X9 undulator-based beamline at the National Synchrotron Light Source. An incident X-ray beam of energy 13.5 keV (wavelength = 0.0918 nm) was collimated using a two-slit system and focused to a beam 100 μm wide by 60 μm tall at the sample position using a Kirkpatrick–Baez mirror system. Samples were mounted inside a small humidity-controlled chamber with Kapton windows.

Grazing-incidence experiments were performed over a range of incidence angles, both below and above the film–vacuum critical angle. Two-dimensional scattering images were measured using a charge-coupled device (CCD) detector. Data conversion to q -space was accomplished using silver behenate powder as a standard.

PM-IRRAS Sample Analysis. The PM-IRRAS measurements were performed on a Nicolet 6700 Fourier transform infrared spectrometer equipped with an external tabletop optical mount. The optical mount was configured with a photoelastic modulator (PEM) with a modulation frequency of 50 kHz, a synchronized sampling demodulator, and a mercury cadmium telluride-A detector. Thin film samples prepared for PM-IRRAS were mounted on a J.A. Woollam HTC-100 hot stage. The hot stage was equipped with a vapor chamber that was used to control temperature and humidity. The humidity within the chamber was tuned by adjusting the flow rates of dry and humidified air, which were premixed before entering the vapor chamber.

The IR spectra were recorded with Omnic software, and the PEM half-wave retardation was set at 4500 cm^{-1} . Four scans were coadded and averaged for each spectrum with a resolution of 32 cm^{-1} , and the beam incident angle was set to 70° to maximize the signal-to-noise ratio. The amount of absorbed water within the Nafion films was based on the absorbance at ~ 3480 cm^{-1} . The advantage of using the polarization-modulation technique is that the random noise from moisture in the surrounding environmental chamber is effectively suppressed. Therefore, the absorbance measured at 3480 cm^{-1} is only due to the absorbed water within the Nafion film. Another distinct advantage of the PM-IRRAS in comparison to conventional IRRAS is that a reference sample is not required for these measurements. This reduces experimental error due to sample changing. An in-depth description of PM-IRRAS technique can be found in the literature.⁶⁴

Typically PM-IRRAS is used to characterize thin films on the order of tens of nanometers or less.⁶⁴ For most organic materials, the linearity in signal intensity does not hold when films are more than 100 nm because these materials tend to experience large thickness or optical constant changes during physical processes such as swelling or shrinking. Simulations based on the study provided by Ochi et al.²² demonstrate that linearity exists for Nafion films on the order of hundreds of nanometers as long as film swelling is relatively low (0–50%). In addition, the refractive indices of Nafion and water do not differ significantly near the observed band region; thus, it is expected that the optical constants during water absorption/diffusion in Nafion are not significantly changed.

Quartz Crystal Microbalance (QCM). Silicon dioxide-coated AT-cut, 14 mm diameter, 4.95 MHz quartz crystals were purchased from Q-Sense (Sweden). Measurements were conducted using a Q-Sense E4, which has a variable data acquisition rate and a maximum mass sensitivity of 0.5 ng/cm^2 . Humidity in the QCM sample chamber was controlled using a mass flow control system similar to the one described in the SXR experimental description. Thin films were prepared by spin-coating directly on the Q-Sense crystals with a silicon oxide surface treatment (to mimic the native oxide of silicon in all of the reflectivity experiments) following the same procedure used for SXR sample preparation. Films were stored under ambient conditions until measurement, typically less than 24 h. The initial dry mass of Nafion was determined by allowing the film to equilibrate under dry nitrogen until the resonance frequency was stable. Water sorption was determined at various relative humidity levels by relating changes in the resonance frequency to mass uptake using the Sauerbrey equation:

$$\Delta f = -\frac{2f_0^2}{A\rho_q v_q} \Delta m \quad (1)$$

where Δf is the frequency change, f_0 is the resonance frequency, Δm is the mass change, A is the piezoelectrically active crystal area, ρ_q is the quartz density, and v_q is the transverse wave velocity in quartz.

RESULTS

SXR Analysis of Equilibrium Water Absorption in Nafion. Information about the absorption of water and the resulting change in film thickness and total scattering length density—related to film composition—was determined as a function of relative humidity using SXR analysis. Figure 1 illustrates the change in the reflectivity as a function of relative humidity for two Nafion films with approximate dry initial thickness values of 30 and 95 nm. Qualitative changes in the fringe frequency and the low- Q reflectivity, affected by the film composition, are both observed. The insets illustrate these changes using the critical edge of silicon as a point of reference (depicted as a vertical line). As the relative humidity increases, there is an increase in the fringe frequency indicating an increase in the film thickness, consistent with water absorption and the subsequent swelling of the films. While it is more difficult to visually discern, there are also changes in the critical edge, Q_c , of the Nafion film as it swells with water, which relates to the film composition. By fitting the reflectivity data with an appropriate model, one can obtain composition information from changes in the scattering length density. The resulting change in the film thickness, scattering length density, and surface roughness can be quantified through the least-squares fitting of the reflectivity data as described in the Experimental Methods section, and the fits are shown as lines through the data in Figure 1. Changes in film thickness as a function of relative humidity can be used to define a swelling strain, ε_z , using the equation

$$\varepsilon_z = \frac{\Delta h}{h_0} \quad (2)$$

where Δh ($= h_{\text{RH}} - h_0$) is the change in film thickness from the “dry” state at a given RH and h_0 is the initial dry film thickness. While ε_z provides a quantitative measure of the swelling, and is certainly important in understanding the response of thin films to environmental conditions, the degree of swelling ultimately reflects the amount of water in the film. In this work our goal is to demonstrate the effect of confinement on fundamental materials properties germane to fuel cell performance; therefore, the solubility of water in these thin films is of critical

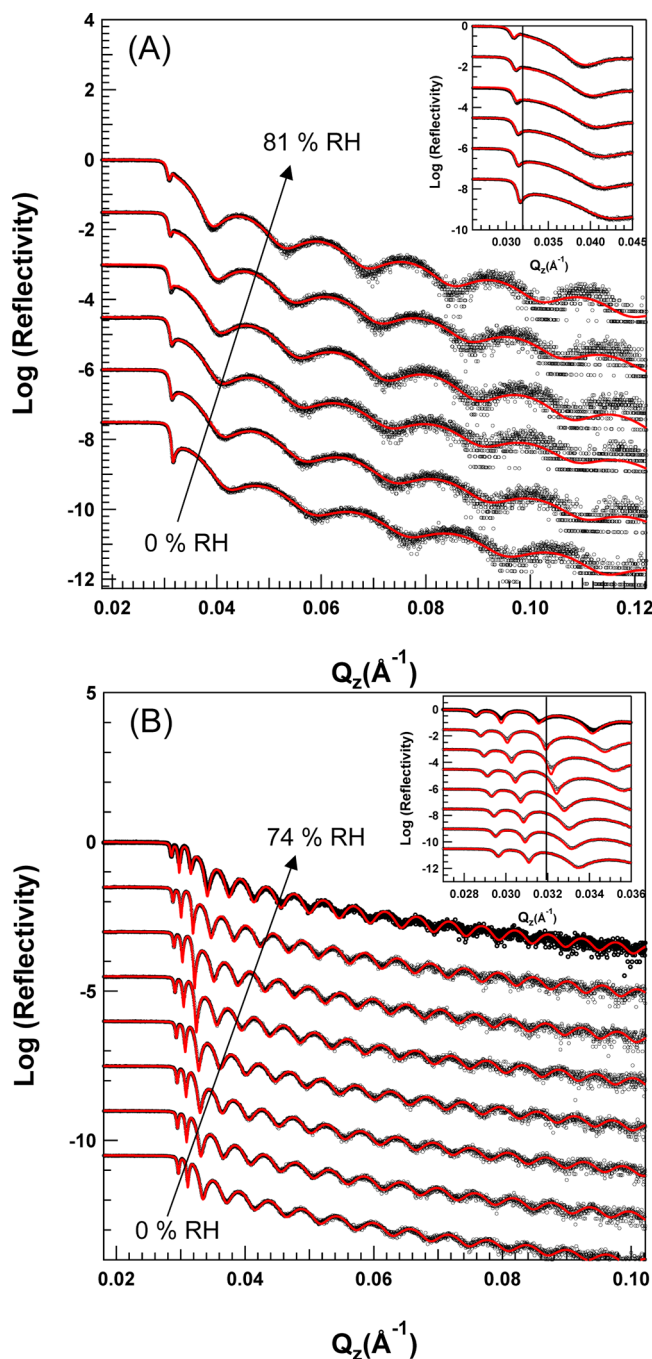


Figure 1. Specular X-ray reflectivity curves for a series of humidified Nafion films with an initial dry film thickness of (A) 30 nm and (B) 95 nm supported a silicon wafer with a layer of native SiO_x .

importance. It is possible to quantify the volume fraction of water uptake from changes in the scattering length density determined from model fits of the scattering intensity. The total scattering length density of the film ρ determined at a given RH is, to a first approximation, interpreted as a linear combination of the scattering length density of the individual components scaled by their relative volume fractions

$$\rho = \sum \phi_i \rho_i = \phi_n \rho_n + \phi_w \rho_w \quad (3)$$

where ϕ_n and ϕ_w represent the volume fractions of Nafion and water, respectively, and the corresponding scattering length densities, ρ_n and ρ_w . The scattering length density of dry Nafion

(ρ_n) was taken to be $\sim 8.48 \times 10^{-4} \text{ \AA}^{-2}$, the value measured for the Nafion films after being dried in the SXR sample chamber overnight ($\phi_w \approx 0$). This value is in close agreement with the scattering length density ($\rho_n = 8.16 \times 10^{-4} \text{ \AA}^{-2}$) calculated from the chemical structure of 1100 EW Nafion and assuming a density of 1.98 g/cm^3 . The scattering length density of pure water ($\rho_w = 4.76 \times 10^{-4} \text{ \AA}^{-2}$) was calculated using the chemical structure and mass density of 1.00 g/cm^3 . Knowing the scattering length densities for each of the components and the total scattering length density, ρ , of the film—as determined from the fit—it is possible to determine the volume fraction of water by rearranging eq 3.

Figure 2A shows the swelling strain as a function of relative humidity for Nafion films ranging from 20 to 222 nm thick. Above 60 nm, the swelling response appears to be largely independent of film thickness. However, a transition in the humidity-dependent swelling response appears below 60 nm. This effect is more apparent when the swelling strain, normalized by the maximum value, is plotted against the initial dry film thickness values for a range of relative humidity values (Figure 2B). While it is clear that the swelling behavior is affected by confinement of Nafion to thin films, particularly thinner than 60 nm, the model used to fit the SXR data is relatively simple and does not consider interfacial structures that have been reported for Nafion films on hydrophilic SiO_x surfaces based on neutron reflectivity (NR) measurements.^{51,52} In order to confirm that the swelling behavior is not significantly affected by interfacial structures, neutron reflectivity was carried out on films of approximately 36 and 159 nm at 88% RH (Figure 3). The broad peak at about $Q = 0.17 \text{ \AA}^{-1}$ is argued to arise from lamellar structures at the interface. The inset of Figure 3 confirms that the lamellar ordering of the water-rich domains does exist in both the thick and thin Nafion films in the region near the SiO_x substrate. It is important to note that this does not indicate a lamellar layering throughout the thickness of the film as will be demonstrated by the GISAXS results. These data do show that at least very near the SiO_x substrate the ionic domains are parallel to the substrate. Nevertheless, when this interfacial structure is taken into consideration when calculating the swelling strain, the NR response is very consistent with the data determined by SXR (Figure 2B). The suppression of the overall swelling of the Nafion films due to thin film confinement is independent of the interfacial structure. In general, these results demonstrate that confining Nafion to a film thickness less than 60 nm suppresses the amount of total swelling that occurs at a given relative humidity.

Ultimately, the swelling is related to the amount of water in the film. Therefore, we have determined the volume fraction of water in the films as a function of RH and initial film thickness using the scattering length density as described in eq 3, to gain further insight into how the solubility of water in Nafion is affected by confinement to thin films. The results of this analysis are shown in Figure 4. Figure 4A shows an increase in the amount of water as a function of RH for all films, which is typical for Nafion membranes. However, below $\sim 60 \text{ nm}$, there is a significant decrease in the solubility of water in the Nafion films. This behavior is demonstrated quite clearly in Figure 4B. To verify this result, the mass fraction of water uptake was measured with QCM and converted to volume fraction. Figure 4B shows that the results determined from SXR correlate very well with those determined by QCM. The solubility of water in Nafion appears to decrease for films thinner than 60 nm. As will

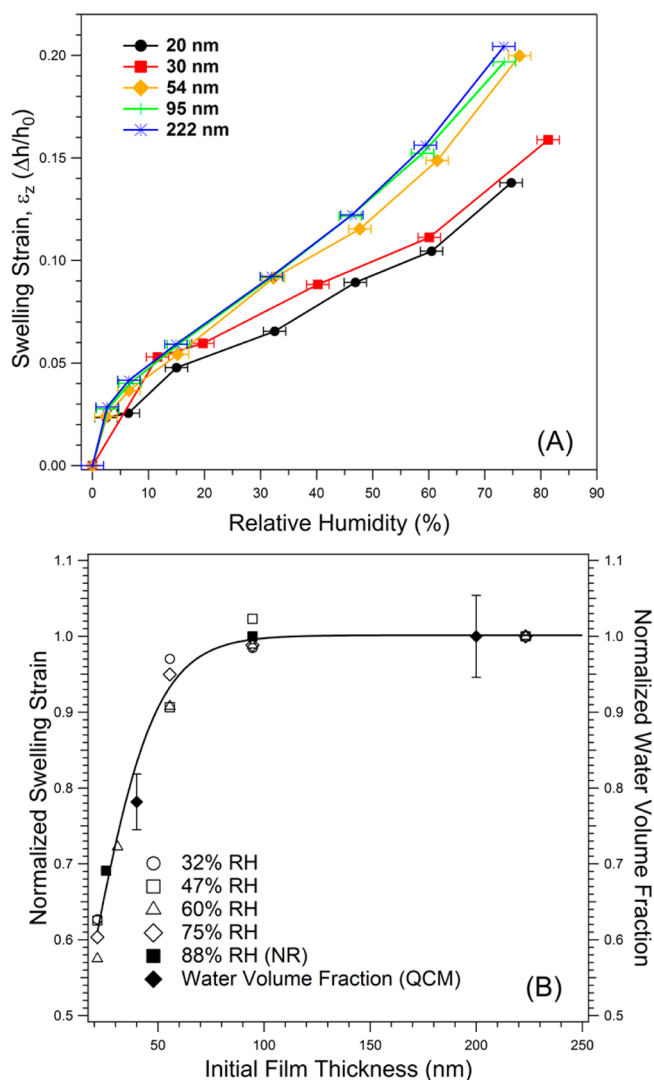


Figure 2. (A) Swelling strain measured for Nafion films of $h = 20$ (●), 30 (■), 54 (◆), 95 (+), and 222 nm (*) as a function of relative humidity. (B) Normalized swelling ratio as a function of initial film thickness at various humidity conditions. Symbols indicate the relative humidity of the environmental chamber: 32% (○), 47% (□), 60% (△), and 75% (◇). The line is presented as a guide to the eye. We have also included the results from neutron reflectivity (■), which take into account structures at the interface. Standard error for the swelling ratio and initial film thickness are within the bounds of the graphical data markers. The water solubility determined from fitting the X-ray reflectivity data is comparable to that determined from QCM (◆) measurements, where the error bars represent standard error from three measurements.

be discussed in more detail below, we also observe a concurrent change in morphology accompanying the solubility change in films less than 60 nm thick. We do not expect any change in specific polymer/water interactions as a function of thickness. However, in addition to the interplay of morphology and water uptake, it is likely that macromolecular confinement is impacting the ability of the water to swell the polymer.

When addressing the issue of reduced swelling/water absorption with decreasing film thickness, it is important to consider the influence that the underlying substrate has on the observed behavior. From a purely mechanical perspective, these films are geometrically confined due to the fact that they are on a solid support or substrate. This restriction affects the stresses,

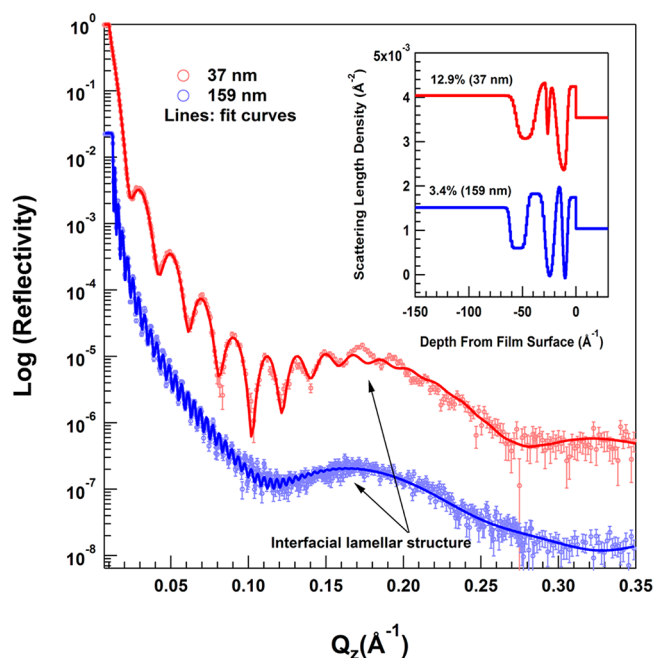


Figure 3. Neutron reflectivity results for two film thicknesses (determined at ca. 88% RH). The broad peak is thought to arise from interfacial lamellae-like structures as shown in the inset.

especially at the interface, which can impact the swelling mechanics. An analysis of ϵ_z as a function of ϕ_w was carried out and was shown to deviate from isotropic swelling of the thin films. The analysis indicates that there is geometric confinement due to the fact that films are supported on a solid substrate. Details of the analysis can be found in the Supporting Information. The main point to be stressed by this analysis is that all of the films, regardless of film thickness (in this range), experience the same level of geometric confinement due to the contact with a solid substrate. From this we can conclude that the confinement effects, or suppression, observed for the swelling strain in the z -direction and the water uptake are not due to stresses because of the confinement of the films to a substrate, but rather that the effects are a result of macromolecular and morphological confinement of the system to thin films.

There are well-documented changes in the physical and transport properties of polymers when confined to films on the order of 50 nm.^{37,39–45,65–67} This idea has been recently demonstrated with Nafion by Dishari and Hickner.⁵⁴ Using a mobility sensitive fluorescent probe, they found that confinement of Nafion to thin films resulted in a decrease in local mobility. While the thinnest films presented in Hickner's work were on the order of 70 nm, their data suggest that significant confinement begins to affect the film properties at this length scale compared to thicker samples. This result is of considerable significance given the results presented here. This information is critical for understanding transport in these materials and will be discussed in the following section.

While we have presented detailed measurements of the water solubility in thin Nafion films, and the subsequent swelling, in order to develop a comprehensive understanding of the thin film behavior of Nafion it is also necessary to probe structural changes as a function of film thickness. It is well-known that the nanostructure is intimately related to water absorption and transport in Nafion. An understanding of how the structure is

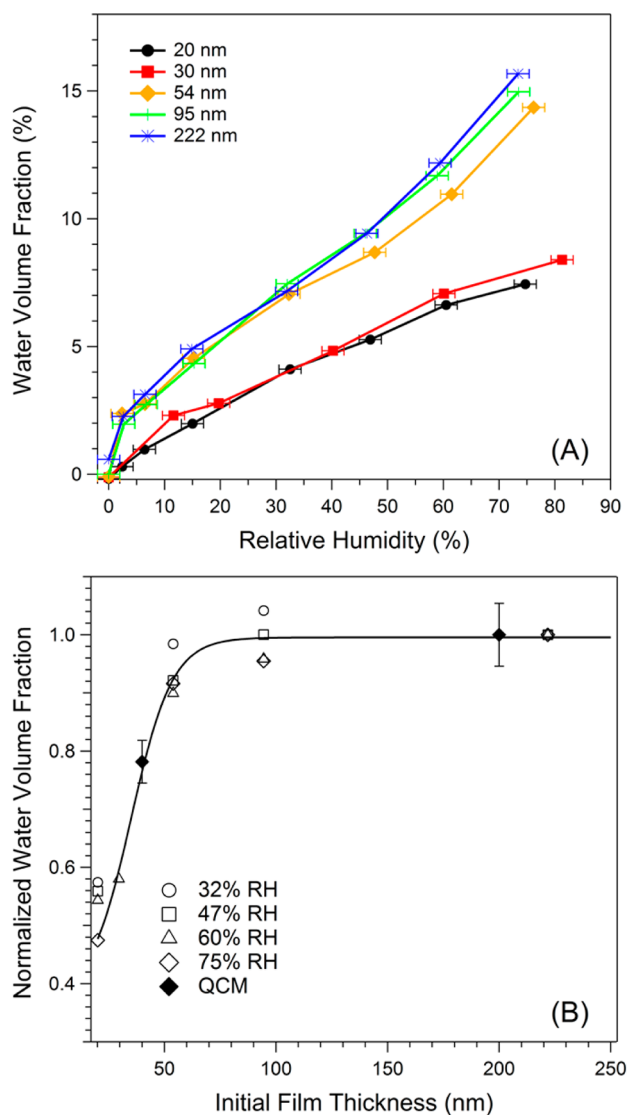


Figure 4. (A) Water volume fraction determined from XR for Nafion films of $h = 20$ (●), 30 (■), 54 (◆), 95 (+), and 222 nm (*) as a function of relative humidity. (B) Normalized swelling ratio as a function of initial film thickness at various humidity conditions. Symbols indicate the relative humidity of the environmental chamber: 32% (○), 47% (□), 60% (△), and 75% (◇). The line is presented as a guide to the eye. Standard error for the swelling ratio and initial film thickness are within the bounds of the graphical data markers. The water solubility determined from fitting the X-ray reflectivity data is comparable to that determined from QCM (◆) measurements, where the error bars represent standard error from three measurements.

affected by confinement can lend insight into the origins of the suppression in water solubility or uptake.

Thin Film Nanostructure by GISAXS. Recently, GISAXS measurements have proven effective in characterizing the internal nanostructure of Nafion thin films on various substrates.^{49–53,68} Here we use the GISAXS technique to show that the internal nanostructure is highly dependent on film thickness. A typical scattering pattern taken at an incident angle just above the critical angle ($\theta_c \approx 0.12^\circ$) is shown in Figure 5. At this incident angle, information about the average structure in the entire thin film is obtained. The scattering peak between 0.15 and 0.20 \AA^{-1} is due to the correlations (i.e., scattering) between the ionic domains and is commonly

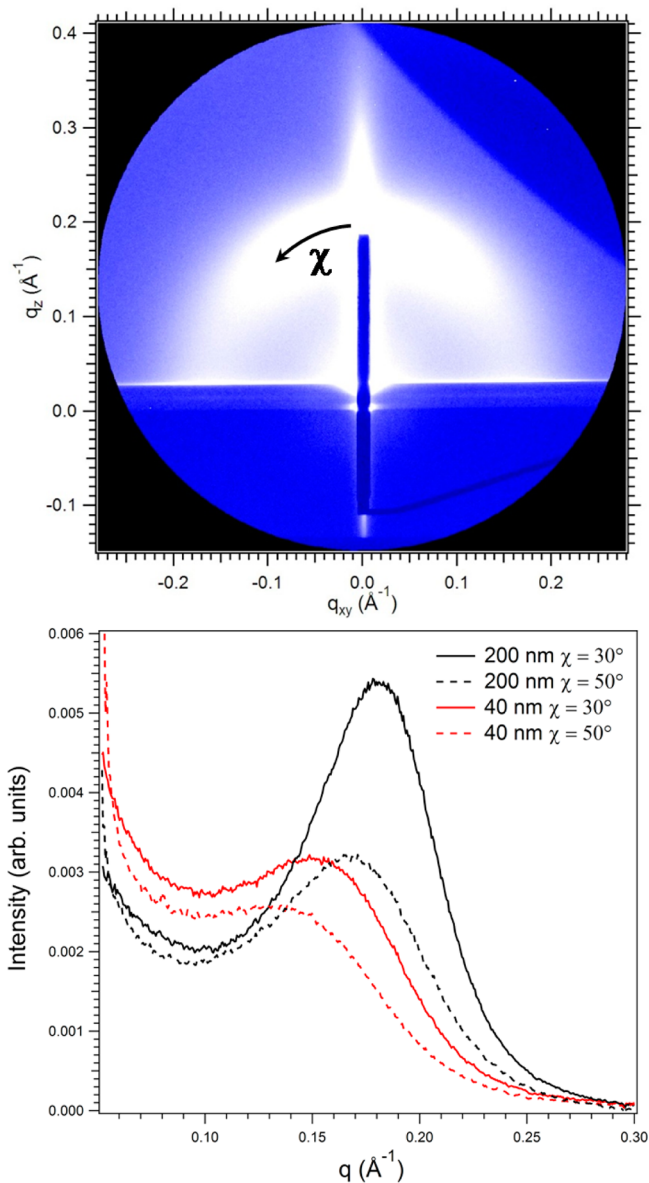


Figure 5. A representative GISAXS detector image (200 nm film equilibrated at ca. 80% RH). The graph indicates the scattering intensity as a function of the scattering vector, q , taken as radial integrations at azimuthal angles of 30° and 50° for a 40 and 200 nm film (both equilibrated at 80% RH). Scattering data were taken just above the critical angle of the film.

referred to as the “ionomer” peak. Comparing the intensity profiles as a function of the scattering vector, q , for the 200 and 40 nm films at an azimuthal angle, χ , of 30° reveals that at 80% RH there is a measurable difference in the ionomer peak position, q_{max} . The calculated d -spacing from the peak is ~ 3.7 nm for the 40 nm film and 3.3 nm for the 200 nm film, respectively. This indicates that the spacing between the aggregates is slightly larger in the thinner film. For comparison, bulk Nafion exhibits Bragg spacing of 3–5 nm, depending on the sample history and testing conditions.⁶⁹ Typically, reports in the literature (which to date have not included film thickness effects) suggest that the d -spacing of the ionomer peak should increase with water content. The larger d -spacing for the thinner films therefore seems to contradict the X-ray reflectivity, neutron reflectivity, and QCM results that the

thinner films absorb less, not more, water. Here, the simple interpretation based on the aggregate spacing does not seem to work. Therefore, we have analyzed the intensity distribution of the ionomer peak and the peak width as a function of the azimuthal scattering angle χ , as defined in Figure 5, for both the humidified thick and thin films.

Figures 5 and 6 reveal anisotropy in the scattering and structure as a function of χ , respectively. The scattering

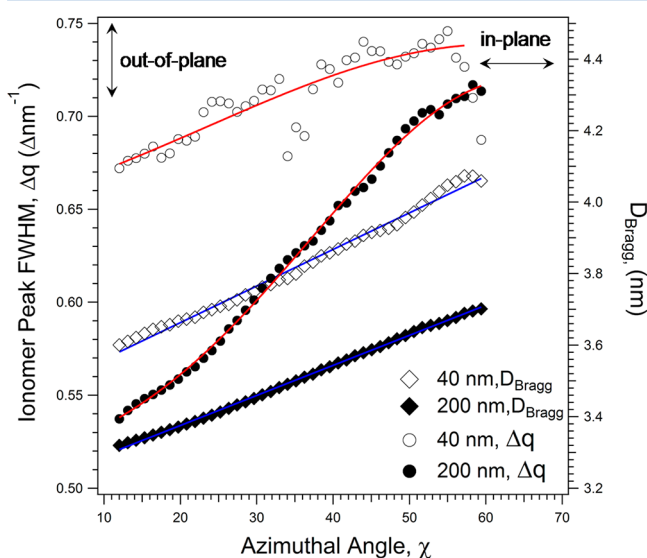


Figure 6. Grain size and Bragg spacing analysis as a function of azimuthal angle, χ , for the GISAXS scattering patterns for 40 and 200 nm films. The scattering was measured *in situ* at a relative humidity of $\sim 80\%$. Lines are present to serve as a guide for the eye. The standard error in the fwhm and the d -spacing is on the order of 5%.

intensity and width of the ionomer peak at various values of χ correspond to various orientations of the correlations and structure of the ionic domains. At low values of χ the scattering is more sensitive to correlations/structure of the ionic domains in the z -direction or out-of-plane. As χ increases, the scattering is affected more by the in-plane correlations and structure of the ionic domains. We have performed an analysis of the distribution of the scattering intensity as a function of χ and found that the intensity distribution is comparable for the two films. In addition, when moving from the out-of-plane (low χ) to in-plane (high χ) orientations, the d -spacing (D_{Bragg}) of the ionic domains systematically increases for both the thick and thin films. These data indicate that the overall orientational order of the aggregates is comparable in the two films, meaning that the average aggregate orientation is similar. However, this does not provide a deeper insight into the observed water uptake trends considering the fact that, traditionally, an increase in D_{Bragg} is correlated to higher water uptake. To gain further insight into the effect of confinement on the internal nanostructure, we also characterized the peak width (full width at half-maximum, fwhm) of the ionomer peak as a function of χ .⁷⁰ In this approach, the peak width is used to characterize the relative amount of order in the system. The peak width can be affected by many factors including, but not limited to, the distribution of the D_{Bragg} , the length over which the domains are correlated, and fluctuations in domain sizes. In general, it is reasonable to assume that broad peak widths represent a material that is less-well-ordered, or less correlated, than one with very narrow peaks. Therefore, by performing this

analysis as a function of the azimuthal angle, one can qualitatively visualize the degree of order, or correlation, of the ionic domains with respect to the relative orientation to the substrate. As shown in Figure 6, film thickness has a significant impact on the internal film structure and degree of order. It should be noted that the reference vector, or zero, for the azimuthal angle is normal to the plane of the film and substrate. Therefore, as the azimuthal angle approaches zero degrees, the scattering is more sensitive to correlations in the through-film, or out-of-plane, direction, whereas angles approaching 90° are more indicative of in-plane correlations.

Again, the data show that D_{Bragg} of the ionic domains, or aggregates, are larger over all orientations for the 40 nm film compared to the 200 nm. This result is not particularly revealing of the effects of confinement. However, the effects of confinement on the fwhm in the two samples are more apparent. The fwhm for the 40 nm film is relatively uniform and larger than in the 200 nm film, regardless of orientation. Interestingly, the fwhm becomes comparable in the two films for the in-plane correlations. These results indicate that while the average d -spacing for the films is slightly different in the in-plane direction, the relative degree of order is comparable. This result is reasonable considering both films experience the same level of in-plane confinement and swelling parallel to the substrate is equally confined by the rigid silicon substrate in both the thick and thin films. However, large differences in fwhm arise for the out-of-plane correlations, which is where one would expect the largest effects of confinement. It appears that in the thicker, less-confined films the ionic domains are able to assume a more ordered structure, likely correlated over larger distances in the thickness direction. However, as the film is confined below 60 nm, the packing of the ionic domains become frustrated. The ionic domains contain less water, are spaced further apart, and are correlated over shorter distances or are less-well-ordered. The effect of confinement on ionic aggregate formation and packing is not unprecedented, as demonstrated by recent work from Kim et al.⁷¹ This work explored the morphology of a series of diblock copolymers consisting of a randomly sulfonated polystyrene block and a hydrophobic polymethylbutylene block. The block copolymers were exposed to humid air, and *in situ* small-angle neutron scattering was used to characterize the overall block copolymer morphology as well as the ionomer morphology within the sulfonated polystyrene domains. Of particular relevance to the work presented here was the effect that confinement of the ionomer block had on the formation of aggregates. It was discovered that when the length scale of the block copolymer structure was less than 10 nm, the ionomer peak associated with ionic aggregates within the sulfonated polystyrene phase was no longer present, thus demonstrating that confinement can play a significant role in the development of ionomer structure and the ability of ionic groups to form aggregate structures.

The fundamental difference in order and packing of the ionic domains in this study lends insight into molecular and structural origins of the suppression of water solubility. A later publication will explore, in more detail, the effect of film thickness and annealing on the structural properties of these materials. The observed differences in structure have implications for water transport and will be discussed in further detail below.

Thickness-Dependent Diffusion by PM-IRRAS. It is well documented that the diffusion of water in Nafion is mostly non-

Fickian, especially during the transition period from a dry state to a fully humidified state.^{16,17,20,21,23} A simple Fickian model does not fully capture the water diffusion kinetics dependence on film thickness, temperature, absorbed water concentration, or different humidity differentials (initial humidity versus final humidity). However, if the humidity differential is relatively low (0% RH to 45% RH), a Fickian diffusion model is reasonably sufficient to describe the effective diffusion kinetics for individual hydration events on a single film and humidity differential as characterized by PM-IRRAS. Therefore, to compare trends with film thickness on the water transport in Nafion, a simple Fickian model was used to parametrize an effective diffusion coefficient. Temperature (25 °C) and humidity differential (0–45% RH) were fixed for all PM-IRRAS experiments to minimize kinetic variations due to environmental conditions. Other factors may contribute to the measured effective diffusion coefficient, including interfacial mass transport,^{20,21,72} and will be discussed further below.

In the Fickian model, the diffusion coefficient is described by the mathematical expression

$$\frac{\partial C}{\partial t} = D_{\text{eff}} \frac{\partial^2 C}{\partial x^2} \quad (4)$$

where C is the water concentration inside the Nafion film at a given distance x into the sample and D_{eff} is the effective diffusion coefficient. For the thin film geometry used in these experiments, it is assumed that initial water concentration in the Nafion film is zero. The water concentration at the Nafion/vapor interface is fixed by the constant relative humidity of the surrounding environment. At the Nafion/air interface, we assume that the water concentration rapidly reaches equilibrium with the water concentration of the surrounding atmosphere. This assumption can be justified by using a high gas flow rate to minimize mass transport limitations near the Nafion film surface, as demonstrated by Elabd et al.^{16,17}

All films were dried by purging the sample chamber with dry nitrogen at room temperature for at least 10 min prior to starting the experiment in order to remove as much water from the film as possible. To ensure that we have sufficiently dried the films, IR spectra are taken until the indicative peak of absorbed water at 3480 cm^{-1} is no longer detected. This drying step satisfies the initial condition of the Nafion film and keeps the concentration differential consistent. We have observed that residual water content can influence the kinetics of water diffusion through the Nafion films, consistent with observations reported in the literature,^{16,17} and have taken efforts to minimize this effect.

After the film was dried, the sample chamber was exchanged with humidified air that flows over the sample throughout the experiment. The relative humidity was simultaneously monitored with a fast response humidity meter, downstream from the sample chamber. IR spectra were recorded at two second intervals starting just before humidified air was exchanged into the sample chamber and collected until the intensity of the water peak at 3480 cm^{-1} remained constant. Since the sample chamber does not reach its humidified state instantaneously, the time constant for the equilibration of the sample chamber to constant relative humidity (0–45%) was accounted for when fitting the kinetic data for water absorption in the films. This was done using a MATLAB algorithm that deconvolutes the sample chamber equilibration response from the observed numerical solution of the Fickian differential equation. The result is an effective water absorption response of the Nafion

film itself. The resulting solution was then analyzed using a least-squares algorithm to determine the effective diffusion coefficient.

Figure 7 shows the time evolution of the water IR band at 3480 cm^{-1} during the hydration process for a 100 nm thick

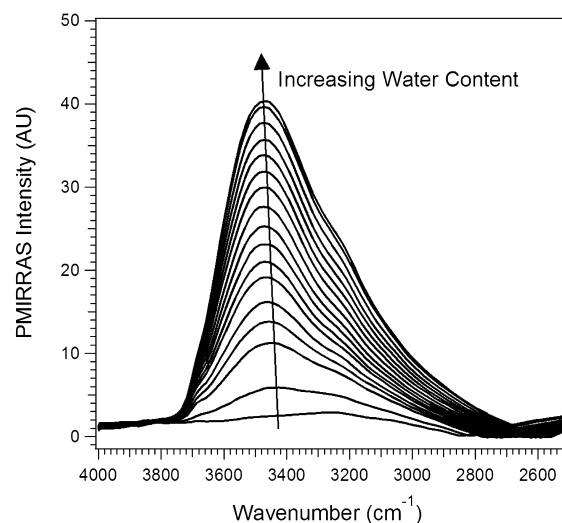


Figure 7. Representative hydration data depicting the evolution of water absorption at 3450 cm^{-1} into a 100 nm film over time.

Nafion film. For convenience in interpreting the analysis, the water band intensity was normalized to its equilibrium value. The kinetic data were plotted as normalized intensity versus the square root of diffusion time scaled by film thickness as shown in Figure 8. For Fickian diffusion into a planar film, the square

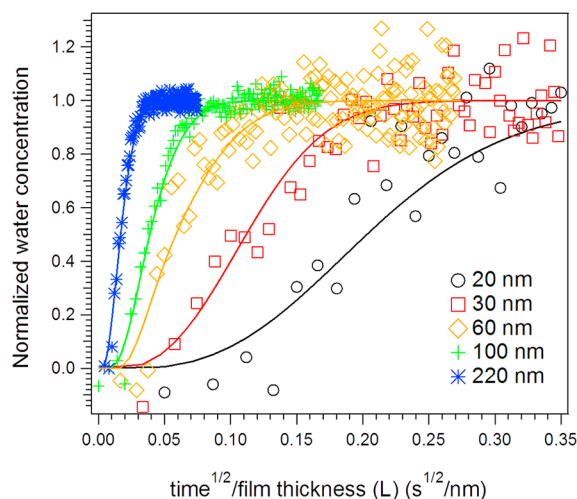


Figure 8. Representative plots of water absorption kinetics of Nafion films of $h = 20$ (○), 30 (□), 60 (◇), 100 (+), and 220 nm (*). Solid lines indicate theoretical fits to the experimental data. Standard errors are within the bounds of the graphical data markers.

root of the diffusion coefficient is proportional to the slope of the initial linear portion of the curve. However, to obtain a more accurate value of the effective diffusion coefficient, the entire kinetic curve was fit through numerical analysis. The kinetic data were also analyzed by scaling the time axis by the film thickness, L , and the square of the thickness. If diffusion was the rate-limiting step for sorption and the internal diffusion

coefficient were thickness independent, then scaling by $1/L^2$ would collapse the kinetic data onto a master curve; on the other hand, if the transport were strictly governed by interfacial mass transport, then the same would occur when scaled by $1/L$. However, neither scaling results in a collapse of the sorption kinetics onto a single curve. It is possible that two factors are contributing to the thickness-dependent transport. First, there is a contribution from interfacial transport resistance, but there is also significant evidence in the literature^{39,40,54,55} to suggest that there are restrictions in the internal diffusion due to confinement effects.

Figure 9 shows the effective water diffusion coefficient as a function of initial, dry film thickness. It has been well

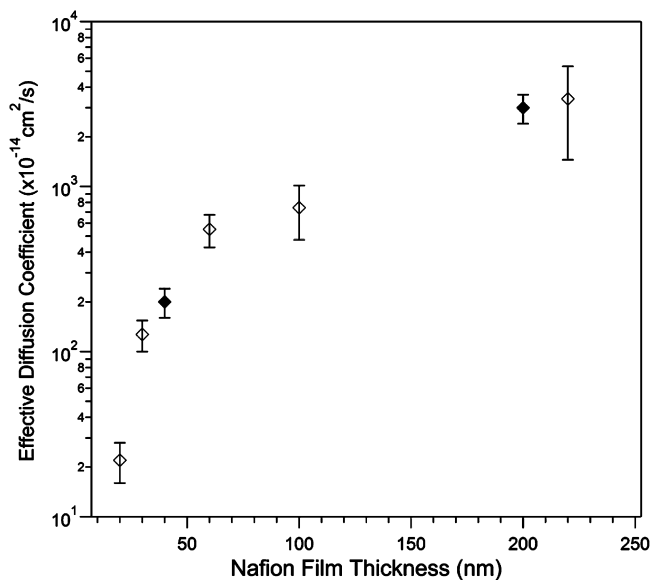


Figure 9. Effective diffusion coefficients of water calculated from kinetic data as a function of initial film thickness as obtained by PM-IRRAS (\diamond) and QCM (\blacklozenge). Standard error for film thickness is within the bounds of the graphical data markers. Error bars for the effective diffusion coefficient are based on the standard error of the fitting of the water concentration.

documented that for bulk membranes the water diffusion through Nafion is dependent on membrane thickness.^{20,21,23,72} A similar trend is observed for thin films; however, there is a clear transition around 50–60 nm where the decrease in water transport kinetics is much more pronounced with decreasing thickness. The film thickness at which this water diffusion transition occurs is consistent with the critical thickness observed in the SXR experiments where trends in water absorption transition from a bulk-like to confined response. This agreement suggests that the observed transition in transport, absorption, and swelling are affected by a similar mechanism. These results are consistent with other works on the water transport in thin films of Nafion and other hydrophilic polymers.^{2,39,40,56} We suspect that the observed behavior is dictated by restricted mobility of the polymer due to macromolecular confinement in addition to changes in the nanostructure caused by confinement. As previously discussed, the GISAXS results show that the nanostructure is affected by confinement. The fact that the ionic aggregates, especially in the out-of-plane direction, are less well-defined for thinner films is to a first approximation consistent with the fact that the transport kinetics appears to be hindered by confinement.

DISCUSSION

It is well understood that the effective diffusivity and solubility of water in Nafion membranes have a significant bearing on the performance (i.e., proton conductivity) and water management within a working fuel cell. While there is a relatively firm understanding of these materials properties for bulk membranes, less is known about how the polyelectrolyte behaves when confined, as is the case in the catalyst layer. Herein we have presented a simplified methodology to start to address these issues. The results presented here demonstrate that the permeability (the product of the solubility and the diffusivity) of water in Nafion can be impacted significantly when the material is confined to dimensions less than 60 nm. This information is critical when attempting to model and understand the transport properties and performance of composite catalyst layer structures. Moreover, these materials properties are ultimately connected to the internal nanostructure of the thin films, which is also influenced by confinement. It should be noted that the films used in this study were prepared in a very different manner, regarding annealing, than those used to prepare bulk films that are used as the electrolyte in a working fuel cell. Thermal treatment has a significant and measurable impact on morphology and transport. The present work seeks to capture the film properties in the as-cast state, and future work will explore the effect of annealing temperature on the morphology and transport in these materials. At this point, it is not clear why confinement effects become significant in the film thickness range of 60 nm, but further studies on the effect of annealing and film thickness on the mechanical response of these materials will lend deeper insights into this phenomenon. However, the current work provides a starting point for describing a mechanism to explain the observations that the proton conductivity and water transport are suppressed in Nafion thin films.^{19,56,58,59}

CONCLUSIONS

Utilizing specular X-ray reflectivity (SXR), neutron reflectivity (NR), grazing-incidence small-angle X-ray scattering (GISAXS), polarization-modulation infrared reflection–absorption spectroscopy (PM-IRRAS), and quartz-crystal microbalance (QCM) measurements we have measured the equilibrium structure, water content, extent of swelling, and effective diffusion coefficient of water in a series of Nafion thin films (20–222 nm) exposed to water vapor. We have demonstrated the effect that confinement has on the aforementioned properties, which are critical for fuel cell catalyst layer performance. Water absorption and film swelling increase as a function of relative humidity, as expected. However, a clear transition in material response is observed around 60 nm. Below this thickness, the swelling and water solubility in Nafion are suppressed compared to films thicker than 60 nm. A similar transition is observed for the water transport, as determined by an effective diffusion coefficient. In addition, it has been shown that the nanostructure, as determined by GISAXS, is greatly affected by film thickness. More specifically, the aggregate spacing was shown to be slightly larger in thinner films and the distance over which the aggregates are correlated is not uniform. In films less than 60 nm, the correlation lengths are smaller, especially in the through-film direction, which could significantly impact water transport through the film. The observed transition in material properties below 60 nm are attributed to confinement of the polymer film. More

importantly, this study alludes to a length scale of the interfacial region affected by the underlying substrate and presents a clear indication that Nafion properties near an interface, or confined to a thin film, significantly differ from bulk behavior. This study also provides a closer approximation to the real values for water absorption and diffusion experienced within a fuel cell as many device simulations are currently based on bulk material properties.

■ ASSOCIATED CONTENT

Supporting Information

Discussion of swelling strain and Figure S1. This material is available free of charge via the Internet at <http://pubs.acs.org>.

■ AUTHOR INFORMATION

Corresponding Author

*E-mail kirt.page@nist.gov.

Author Contributions

†These authors contributed equally to this work.

Notes

The authors declare no competing financial interest.

■ ACKNOWLEDGMENTS

S. Eastman thanks the National Research Council Postdoctoral Program for their support. The assistance and valuable discussions with Joe Dura and Steve Decaluwe at the NIST Center for Neutron Research and Hae-Jeong Lee in Polymers Division at NIST are also greatly appreciated. Professor Yossef Elabd at Drexel University also provided critical feedback during manuscript preparation. Research was carried out in part at the Center for Functional Nanomaterials and the National Synchrotron Light Source, Brookhaven National Laboratory, which is supported by the U.S. Department of Energy, Office of Basic Energy Sciences, under Contract DE-AC02-98CH10886.

■ REFERENCES

- (1) Cele, N.; Ray, S. S. *Macromol. Mater. Eng.* **2009**, *294* (11), 719–738.
- (2) Kreuer, K. D. *J. Membr. Sci.* **2001**, *185* (1), 29–39.
- (3) Slade, S.; Campbell, S. A.; Ralph, T. R.; Walsh, F. C. *J. Electrochem. Soc.* **2002**, *149* (12), A1556–A1564.
- (4) Nemat-Nasser, S. *J. Appl. Phys.* **2002**, *92* (5), 2899–2915.
- (5) Nemat-Nasser, S.; Wu, Y. X. *Smart Mater. Struct.* **2006**, *15* (4), 909–923.
- (6) Park, J. K.; Moore, R. B. *ACS Appl. Mater. Interfaces* **2009**, *1* (3), 697–702.
- (7) Choi, H. N.; Cho, S. H.; Lee, W. Y. *Anal. Chem.* **2003**, *75* (16), 4250–4256.
- (8) Hrapovic, S.; Liu, Y. L.; Male, K. B.; Luong, J. H. T. *Anal. Chem.* **2004**, *76* (4), 1083–1088.
- (9) Su, P. G.; Sun, Y. L.; Lin, C. C. *Sens. Actuators, B* **2006**, *115* (1), 338–343.
- (10) Equipment and instruments or materials are identified in the paper in order to adequately specify the experimental details. Such identification does not imply recommendation by the National Institute of Standards and Technology (NIST), nor does it imply the materials are necessarily the best available for the purpose.
- (11) Gebel, G. *Polymer* **2000**, *41* (15), 5829–5838.
- (12) Page, K. A.; Cable, K. M.; Moore, R. B. *Macromolecules* **2005**, *38* (15), 6472–6484.
- (13) Page, K. A.; Landis, F. A.; Phillips, A. K.; Moore, R. B. *Macromolecules* **2006**, *39* (11), 3939–3946.
- (14) Schmidt-Rohr, K.; Chen, Q. *Nat. Mater.* **2008**, *7* (1), 75–83.
- (15) Burnett, D. J.; Garcia, A. R.; Thielmann, F. *J. Power Sources* **2006**, *160* (1), 426–430.
- (16) Hallinan, D. T.; De Angelis, M. G.; Baschetti, M. G.; Sarti, G. C.; Elabd, Y. A. *Macromolecules* **2010**, *43* (10), 4667–4678.
- (17) Hallinan, D. T.; Elabd, Y. A. *J. Phys. Chem. B* **2009**, *113* (13), 4257–4266.
- (18) Hensley, J. E.; Way, J. D.; Dec, S. F.; Abney, K. D. *J. Membr. Sci.* **2007**, *298* (1–2), 190–201.
- (19) Krtil, P.; Trojanek, A.; Samec, Z. *J. Phys. Chem. B* **2001**, *105* (33), 7979–7983.
- (20) Majsztrik, P.; Bocarsly, A.; Benziger, J. *J. Phys. Chem. B* **2008**, *112* (51), 16280–16289.
- (21) Majsztrik, P. W.; Satterfield, M. B.; Bocarsly, A. B.; Benziger, J. B. *J. Membr. Sci.* **2007**, *301* (1–2), 93–106.
- (22) Ochi, S.; Kamishima, O.; Mizusaki, J.; Kawamura, J. *Solid State Ionics* **2009**, *180* (6–8), 580–584.
- (23) Satterfield, M. B.; Benziger, J. B. *J. Phys. Chem. B* **2008**, *112* (12), 3693–3704.
- (24) Satterfield, M. B.; Benziger, J. B. *J. Polym. Sci., Part B: Polym. Phys.* **2009**, *47* (1), 11–24.
- (25) Zawodzinski, T. A.; Derouin, C.; Radzinski, S.; Sherman, R. J.; Smith, V. T.; Springer, T. E.; Gottesfeld, S. *J. Electrochem. Soc.* **1993**, *140* (4), 1041–1047.
- (26) Zhao, Q. A.; Majsztrik, P.; Benziger, J. *J. Phys. Chem. B* **2011**, *115* (12), 2717–2727.
- (27) Bazylak, A. *Int. J. Hydrogen Energy* **2009**, *34* (9), 3845–3857.
- (28) Das, S. K.; Bansode, A. S. *Heat Transfer Eng.* **2009**, *30* (9), 691–719.
- (29) Luan, Y. H.; Zhang, Y. M.; Zhang, H.; Li, L.; Li, H.; Liu, Y. G. *J. Appl. Polym. Sci.* **2008**, *107* (1), 396–402.
- (30) Adjemian, K. T.; Lee, S. J.; Srinivasan, S.; Benziger, J.; Bocarsly, A. B. *J. Electrochem. Soc.* **2002**, *149* (3), A256–A261.
- (31) Liu, D.; Yates, M. Z. *J. Membr. Sci.* **2009**, *326* (2), 539–548.
- (32) Su, L. J.; Li, L.; Li, H.; Zhang, Y. M.; Yu, W.; Zhou, C. X. *J. Membr. Sci.* **2009**, *335* (1–2), 118–125.
- (33) Rivin, D.; Kendrick, C. E.; Gibson, P. W.; Schneider, N. S. *Polymer* **2001**, *42* (2), 623–635.
- (34) Mashio, T.; Malek, K.; Eikerling, M.; Ohma, A.; Kanesaka, H.; Shinohara, K. *J. Phys. Chem. C* **2010**, *114* (32), 13739–13745.
- (35) More, K. L. *DOE Hydrogen Program Annual Progress Report*, Nov 2005.
- (36) Huinink, H. P.; Brokken-Zijp, J. C. M.; van Dijk, M. A.; Sevink, G. J. A. *J. Chem. Phys.* **2000**, *112* (5), 2452–2462.
- (37) Roth, C. B.; Dutcher, J. R. *J. Electroanal. Chem.* **2005**, *584* (1), 13–22.
- (38) Fryer, D. S.; Nealey, P. F.; de Pablo, J. J. *Macromolecules* **2000**, *33* (17), 6439–6447.
- (39) Vogt, B. D.; Soles, C. L.; Lee, H. J.; Lin, E. K.; Wu, W. *Polymer* **2005**, *46* (5), 1635–1642.
- (40) Vogt, B. D.; Soles, C. L.; Lee, H. J.; Lin, E. K.; Wu, W. L. *Langmuir* **2004**, *20* (4), 1453–1458.
- (41) Alcoutlabi, M.; McKenna, G. B. *J. Phys.: Condens. Matter* **2005**, *17* (15), R461–R524.
- (42) Forrest, J. A. *Eur. Phys. J. E* **2002**, *8* (2), 261–266.
- (43) Forrest, J. A.; Dalnoki-Veress, K. *Adv. Colloid Interface Sci.* **2001**, *94* (1–3), 167–196.
- (44) Soles, C. L.; Douglas, J. F.; Wu, W. L.; Peng, H.; Gidley, D. W. A broad perspective on the dynamics of highly confined polymer films. In *Polymer Interfaces and Thin Films*; Karim, A., Russell, T. P., Frank, C. W., Nealey, P. F., Eds.; Materials Research Society: Warrendale, PA, 2002; Vol. 710, pp 17–22.
- (45) Stafford, C. M.; Harrison, C.; Beers, K. L.; Karim, A.; Amis, E. J.; Vanlandingham, M. R.; Kim, H. C.; Volksen, W.; Miller, R. D.; Simonyi, E. E. *Nat. Mater.* **2004**, *3* (8), 545–550.
- (46) Torres, J. M.; Stafford, C. M.; Vogt, B. D. *ACS Nano* **2009**, *3* (9), 2677–2685.
- (47) Lange, K. J.; Sui, P.-C.; Djilali, N. *J. Electrochem. Soc.* **2010**, *157* (10), B1434–B1442.
- (48) Masuda, T.; Naohara, H.; Takakusagi, S.; Singh, P. R.; Uosaki, K. *Chem. Lett.* **2009**, *38* (9), 884–885.

- (49) Bass, M.; Berman, A.; Singh, A.; Kononov, O.; Freger, V. *J. Phys. Chem. B* **2010**, *114* (11), 3784–3790.
- (50) Bass, M.; Berman, A.; Singh, A.; Kononov, O.; Freger, V. *Macromolecules* **2011**, *44* (8), 2893–2899.
- (51) Dura, J. A.; Murthi, V. S.; Hartman, M.; Satija, S. K.; Majkrzak, C. F. *Macromolecules* **2009**, *42* (13), 4769–4774.
- (52) Murthi, V. S.; Dura, J. A.; Satija, S.; Majkrzak, C. F. Water Uptake and Interfacial Structural Changes of Thin Film Nafion (R) Membranes Measured by Neutron Reflectivity for PEM Fuel Cells. In *Proton Exchange Membrane Fuel Cells 8, Pts 1 and 2*; Fuller, T., Shinohara, K., Ramani, V., Shirvanyan, P., Uchida, H., Cleghorn, S., Inaba, M., Mitsushima, S., Strasser, P., Nakagawa, H., Gasteiger, H. A., Zawodzinski, T., Lamy, C., Eds.; Electrochemical Society Inc.: Pennington, NJ, 2008; Vol. 16, pp 1471–1485.
- (53) Wood, D. L.; Chlistunoff, J.; Majewski, J.; Borup, R. L. *J. Am. Chem. Soc.* **2009**, *131* (50), 18096–18104.
- (54) Dishari, S. K.; Hickner, M. A. *ACS Macro Lett.* **2012**, 291–295.
- (55) He, L. L.; Smith, H. L.; Majewski, J.; Fujimoto, C. H.; Cornelius, C. J.; Perahia, D. *Macromolecules* **2009**, *42* (15), 5745–5751.
- (56) Kongkanand, A. *J. Phys. Chem. C* **2011**, *115* (22), 11318–11325.
- (57) Sun, L. X.; Okada, T. *J. Membr. Sci.* **2001**, *183* (2), 213–221.
- (58) Siroma, Z.; Ioroi, T.; Fujiwara, N.; Yasuda, K. *Electrochem. Commun.* **2002**, *4* (2), 143–145.
- (59) Siroma, Z.; Kakitsubo, R.; Fujiwara, N.; Ioroi, T.; Yamazaki, S. I.; Yasuda, K. *J. Power Sources* **2009**, *189* (2), 994–998.
- (60) Parratt, L. G. *Phys. Rev.* **1954**, *95* (2), 359–369.
- (61) Anker, J. F. a. M.; J, C. *Proc. SPIE* **1992**, *260*, 1738.
- (62) Kienzle, P. A.; O'Donovan, K. V.; Ankner, J. F.; Berk, N. F.; Majkrzak, C. F. <http://www.ncnr.nist.gov/reflpak>.
- (63) Dura, J. A.; Pierce, D. J.; Majkrzak, C. F.; Maliszewskij, N. C.; McGillivray, D. J.; Losche, M.; O'Donovan, K. V.; Mihailescu, M.; Perez-Salas, U.; Worcester, D. L.; White, S. H. *Rev. Sci. Instrum.* **2006**, *77*, 7.
- (64) Buffeteau, T.; Desbat, B.; Turlet, J. M. *Appl. Spectrosc.* **1991**, *45* (3), 380–389.
- (65) Fukao, K.; Miyamoto, Y. *Phys. Rev. E* **2000**, *61* (2), 1743–1754.
- (66) Keddie, J. L.; Jones, R. A. L.; Cory, R. A. *Europhys. Lett.* **1994**, *27* (1), 59–64.
- (67) O'Connell, P. A.; McKenna, G. B. *J. Polym. Sci., Part B: Polym. Phys.* **2009**, *47* (24), 2441–2448.
- (68) Modestino, M. A.; Kusoglu, A.; Hexemer, A.; Weber, A. Z.; Segalman, R. A. *Macromolecules* **2012**, *45* (11), 4681–4688.
- (69) Mauritz, K. A.; Moore, R. B. *Chem. Rev.* **2004**, *104* (10), 4535–4585.
- (70) Smilgies, D.-M. *J. Appl. Crystallogr.* **2009**, *42* (6), 1030–1034.
- (71) Kim, S. Y.; Park, M. J.; Balsara, N. P.; Jackson, A. *Macromolecules* **2010**, *43* (19), 8128–8135.
- (72) Adachi, M.; Navessin, T.; Xie, Z.; Li, F. H.; Tanaka, S.; Holdcroft, S. *J. Membr. Sci.* **2010**, *364* (1–2), 183–193.